Ore Geology Reviews 105 (2019) 1–17

Contents lists available at ScienceDirect

Ore Geology Reviews

journal homepage: www.elsevier.com/locate/oregeorev

3D computational simulation-based mineral prospectivity modeling for exploration for concealed Fe–Cu skarn-type mineralization within the Yueshan orefield, Anqing district, Anhui Province, China

Xiaohui Li[a,b], Feng Yuan[a,b,c,*], Mingming Zhang[a,b], Simon M. Jowitt[d], Alison Ord[e], Taofa Zhou[a,b], Wenqiang Dai[a,b]

[a] School of Resources and Environmental Engineering, Hefei University of Technology, Hefei, Anhui 230009, China
[b] Anhui Province Engineering Research Center for Mineral Resources and Mine Environments, Hefei University of Technology, Hefei, Anhui 230009, China
[c] Xinjiang Research Centre for Mineral Resources, Xinjiang Institute of Ecology and Geography, Chinese Academy of Sciences, Urumqi, Xinjiang 830011, China
[d] Department of Geoscience, University of Nevada Las Vegas, 4505 S. Maryland Parkway, Las Vegas, NV 89154-4010, USA
[e] Centre for Exploration Targeting, University of Western Australia, Crawley 6008, Australia

ARTICLE INFO

Keywords:
3D modeling
Mineral prospectivity modeling
Computational simulation
Skarn-type deposit
Yueshan orefield

ABSTRACT

The Yueshan orefield is one of the best-known Fe–Cu orefields in China and is located within the central Yangtze metallogenic belt ofin Anhui Province, China. The recent discovery of the skarn-type Zhuchong Fe–Cu deposit at depth within the orefield has highlighted the prospectivity of this area to host deep-seated skarn-type mineralization. However, the effectiveness of traditional geophysical exploration techniques is reduced with increasing depth. This, combined with recent developments in 3D mineral prospectivity modeling has led to the use of a 3D targeting approach for exploration for deep-seated and concealed mineralization in this area. However, to date the usefulness of this approach has been limited by a lack of an approach that could generate more useful 3D predictive maps. This study presents a 3D computational simulation based mineral prospectivity modeling approach that identified several exploration targets for concealed and deep-seated skarn-type mineralization within the Yueshan orefield. These prospective targets include areas of known mineralization as well as a number of new targets for future mineral exploration. In addition, the analysis of the resulting data using a capture-efficiency curve indicates that these 3D computational simulation approaches can provide additional predictive information for mineral exploration, indicating that 3D computational simulation should have a key role in the development and use of future 3D prospectivity modeling techniques during exploration targeting.

1. Introduction

The continuous improvement of geological exploration techniques and methods has led to a significant increase in the amount and type of geoscientific data that is used in mineral exploration. However, this increase in data availability has also generated a number of challenges in terms of how to extract and combine only those data that can effectively be used to predict the location of hitherto undiscovered mineralization (Agterberg et al., 1990; Carranza, 2009; Harris, 1984; Lindsay et al., 2014). One approach that has been refined over the past few decades is mineral prospectivity modeling, an approach that is now widely used for the identification of areas prospective for mineral exploration on a regional scale. This approach that combines and integrates multiple geoscientific datasets, including surficial geology, geophysical data, geochemical data, remote sensing data, and other information (Bonham-Carter, 1994; Carranza, 2004; Yousefi and Carranza, 2016; Zuo et al., 2009). However, mature mining districts that have been the subject of significant amounts of mineral exploration, such as those within eastern China that have been exploited for more than 50 years, are commonly faced with a situation where the vast majority of easy to discover (i.e., outcropping and near-surface) mineral deposits have already been discovered. This means that finding new deposits in these mature mining districts becomes increasingly difficult over time, requiring a new approach that targets deep-seated and concealed ore deposits to replenish depleted reserves in areas that have been exploited for a significant amount of time.

The targeting of deep and concealed ore deposits during mineral exploration is extremely challenging, primarily as a result of the

* Corresponding author.
E-mail address: yf_hfut@163.com (F. Yuan).

https://doi.org/10.1016/j.oregeorev.2018.12.003
Received 16 March 2018; Received in revised form 3 December 2018; Accepted 9 December 2018
Available online 11 December 2018
0169-1368/

inherent increase in complexity when exploring in deeper areas with less dense geological information (Lü et al., 2007). One approach that can provide new insights into exploration targeting at depth is the analysis and modeling of 3D geological objects using an integrated geophysical and geological approach (Lindsay et al., 2012; Li et al., 2015). These 3D mineral prospectivity modeling approaches are based on 3D geological models and have been applied to the exploration targeting of deep-seated and concealed mineralization elsewhere both on regional (Li et al., 2015; Nielsen et al., 2015; Payne et al., 2015; Perrouty et al., 2014; Wang et al., 2015) and deposit (Abedi et al., 2012; Wang and Huang, 2012; Xiao et al., 2015; Yuan et al., 2014a,b) scales. This body of research indicates both the feasibility and usability of 3D mineral prospectivity modeling as well as providing an approach that can be effectively used for mineral exploration at depth. However, compared with 2D mineral prospectivity modeling, 3D mineral prospectivity modeling has always been limited by a lack of availability of 3D predictive maps. Finding and mining information from 3D data and geological models are the most effective and feasible ways to improve the efficiency and accuracy of 3D mineral prospectivity modeling. Recent developments in computational simulation methods such as the incorporation of multi-physics coupling, non-equilibrium thermodynamics and open flow systems that are used to quantitatively study the processes of complex ore-forming systems have also provided new opportunities for future developments in 3D mineral prospectivity modeling (Weis and Heinrich, 2012, Ord et al., 2012a,b; Liu et al., 2012, 2014a,b).

This study focuses on the Yueshan orefield, within the central Yangtze metallogenic belt of Anhui Province, China, an area that is well-endowed with Fe–Cu mineralization and has been the subject of a significant amount of previous research (e.g., Chang et al., 1991; Dong and Qiu, 1993; Liu et al., 2012; Mao et al., 2006a,b; Zhou et al., 2000; Zhou et al., 2005). The exhaustion of the shallow orebodies in this areas has led to increased efforts to target concealed orebodies located at depth. This led to the discovery of the skarn-type Zhuchong Fe–Cu deposits within the northern part of the Yueshan orefield. The majority of this mineralization is located at depths greater than 800 m, indicating that the Yueshan orefield should be considered highly prospective for as-yet undiscovered deep-seated mineralization. The orefield itself is dominated by skarn-type Fe–Cu deposits and this study presents the results of 3D mineral prospectivity modeling of the orefield, an approach that combines 3D computational simulation, 3D geological modeling, 3D geophysical inversion, 3D spatial analysis and 3D data fusion methods to highlight prospective areas for future exploration for deep-seated skarn-type mineralization within the Yueshan orefield.

2. Geological setting

2.1. Regional geology

The Middle–Lower Yangtze Metallogenic Belt (MLYB) is one of the most important Fe–Cu–Au-polymetallic metallogenic belts in China (Chang et al., 1991; Mao et al., 2011; Zhai et al., 1992; Zhou et al., 2015) and is located within the Yangtze tectonic depression along the northern margin of the Yangtze Block. The MLYB is bounded by the Xiangfan–Guangji (XGF) and Tan–Lu (TLF) faults to the northwest and by the Yangxin–Changzhou Fault (YCF) to the southeast (Fig. 1). Prolonged and related tectonic, magmatic, and metallogenic events since the Jinningian (ca. 850–800 Ma) have generated a faulted uplift and depression tectonic framework in this region as well as more than 200 diverse Fe–Cu–Au-polymetallic ore deposits and prospects that are located in a number of mining districts known as ore concentration areas (OCAs). These include the volcanic rift basin-hosted Luzong and Ningwu OCAs and the secondary uplift-hosted Tongling, Anqing-Quichi, Jiurui, Ningzhen and Edongnan OCAs. The MLYB contains diverse ore deposit types (e.g., Chang et al., 1991) that are dominated by the porphyry-, skarn- and magnetite-apatite-type deposits that host the majority of the Cu–Fe–Au mineralization in this area (Fig. 1), all of which are closely associated with the extensive and voluminous Yanshanian tectono-thermal events recorded in this region (Sun et al., 2017; Yuan et al., 2012; Zhou et al., 2015).

2.2. Geology of the Yueshan orefield

The Yueshan orefield is located in the northwest of the Anqing–Guichi OCA (Fig. 1) and records an intense history of folding, faulting and magmatism (Fig. 2). The area contains Silurian to Jurassic sedimentary rocks (Fig. 2) and the mineralization and magmatism in this area was controlled by NNW–SSE trending faults as well as E–W trending faults within Precambrian Dongling Formation (1895 ± 38 Ma) basement in this area (Xing and Xu, 1993; Zhou et al., 2007). The majority of the widespread magmatic rocks in this area were emplaced during the Yanshanian, including the multi-phase diorite–quartz diorite–monzodiorite Yueshan, Zongpu and Wuheng intrusions (Fig. 2). Zircon SHRIMP U–Pb analysis yielded an age of 138.7 ± 0.5 Ma for the Yueshan intrusion (Zhang et al., 2008), whereas zircon laser ablation–inductively coupled plasma–mass spectrometry (LA–ICP–MS) U–Pb dating of the Wuheng intrusion yielded ages of 140.0 ± 1.6 Ma for dioritic samples and 132.9 ± 1.5 Ma for monzodioritic samples (Liu et al., 2014a,b).

The Yueshan orefield contains numerous skarn-type Fe–Cu deposits, the majority of which are associated with the Yueshan intrusion (Fig. 2). The mineralization associated with these deposits is concentrated within the contact zone between the Yueshan intrusion and the surrounding Triassic sedimentary carbonates of the Yueshan (T_2y) and Nanlinhu (T_1n) formations (Fig. 3). The orefield contains some 100 Mt of Fe reserves at a grade of 48% Fe, 0.61 Mt of contained Cu metal at grades between 0.8% and 2% Cu, and over 10 t of contained Au metal at grades between 0.2 and 2.0 g/t Au. The two largest deposits within the orefield are both skarn-type deposits, namely the Anqing Fe–Cu deposit, which has measured reserves of 62.4 Mt at 0.906% Cu and 32.2% Fe (Zhou et al., 2007), and the Zhuchong Fe–Cu deposit, which has measured reserves of 4.39 Mt at 1.15% Cu and 51.63 Mt at 50.10% Fe (326 Geological Team, 2012). Some smaller deposits have also been identified within the contact zone of the dioritic Yueshan diorite intrusion, including the Matoushan Fe–Cu, Liujiadapai Fe, and Liujiawa Fe–Cu skarn-type deposits, the intrusion-hosted porphyry-type Longmenshan Cu and Tongniujin Cu–Mo deposits and the fracture-hosted epithermal Bailin Au deposit.

2.3. Deposit geology

2.3.1. Anqing and Matoushan Fe–Cu deposits

The Anqing Fe-Cu deposit was discovered in the 1960s and is the type example of a Yueshan orefield skarn-type deposit. It is associated with the dioritic Yueshan intrusion, which was emplaced into Middle Triassic littoral to neritic carbonate units that are interbedded with bathyal facies sediments (Fig. 4). The deposit is spatially zoned, with garnet- and magnetite-bearing exoskarns typically occurring within an external zone associated with marble development, whereas diopside- and scapolite- bearing endoskarn and altered diorite-type mineralization is entirely located within the associated diorite intrusion (Zhou et al., 2007). The orebodies that define the Anqing Fe–Cu deposit are tongue-shaped and vary in size, reflecting the size and nature of the contact zone between the dioritic intrusion and the surrounding carbonate country rocks. The skarn orebodies are located at depths of 280–580 m and have an average thickness of 50 m. These orebodies contain magnetite, hematite, chalcopyrite, pyrrhotite, pyrite, molybdenite and bornite within a garnet, pyroxene, wollastonite, albite, actinolite–tremolite, muscovite, chlorite, epidote, sericite, quartz and calcite gangue assemblage.

The skarn-type Matoushan deposit is located close to the Anqing

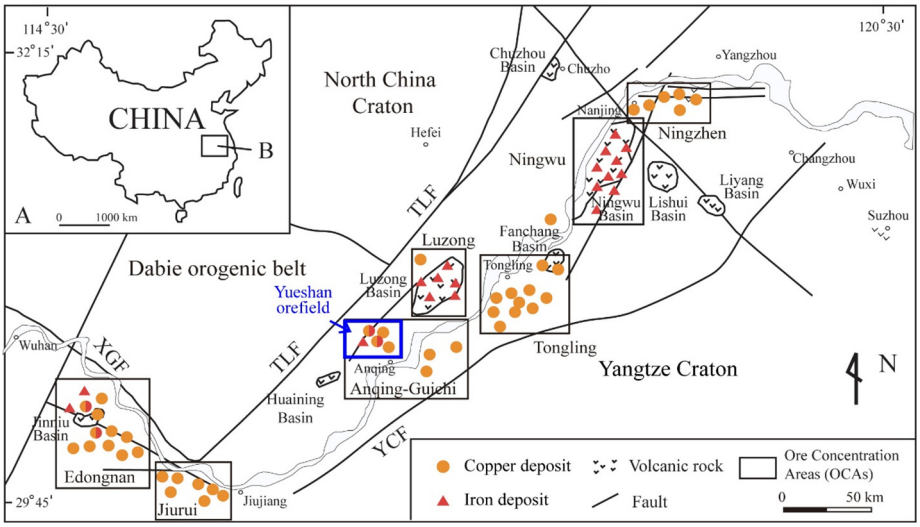

Fig. 1. (A) Map showing the location of the middle and lower regions of the Yangtze Metallogenic Belt, and (B) the location of Yueshan orefield, volcanic basins and ore concentration areas (OCAs) within the middle and lower Yangtze River Metallogenic Belt as well as the location of major settlements, faults and major tectonic features (modified after Chang et al., 1991; Mao et al., 2011).

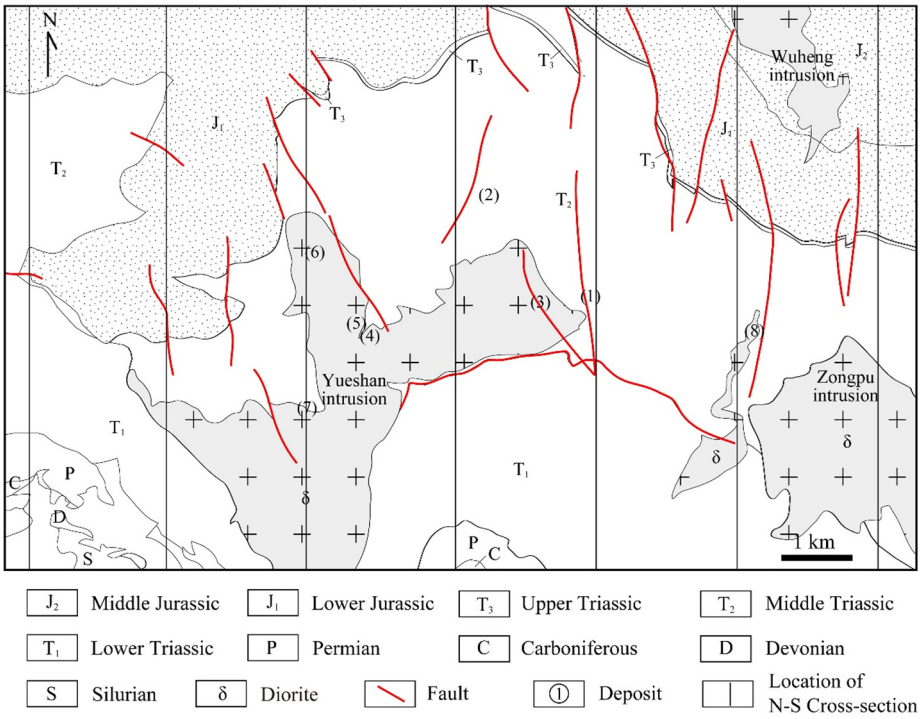

Fig. 2. Geological map of the Yueshan orefield, showing the main geological units, major faults and the location of important mineral deposits as follows: (1)- Anqing Cu-Fe deposit, (2)- Zhuchong Fe-Cu deposit, (3)- Matoushan Cu–Fe deposit, (4)- Longmenshan Cu deposit, (5)- Liujiawa Fe-Cu deposit, (6)- Tongniujin Cu–Mo deposit, (7)- Liujiadapai Fe deposit, (8)- Bailin Au deposit.

Fe–Cu deposit and shares similar geological characteristics and mineral assemblages. The majority of the individual orebodies that define the Matoushan Fe–Cu deposit are also tongue shaped with limits defined by the shape and nature of the contact zone between the surrounding Triassic carbonates and the diorite intrusion (Fig. 5).

2.3.2. Zhuchong Fe–Cu deposit

The skarn-type Zhuchong Fe–Cu deposit was discovered in 2012 and is located in an area containing the Middle Triassic Tongtoujian Formation (T_2t) and underlying units of the Middle Triassic Yueshan (T_2y) and Lower Triassic Nanlinghu (T_1n) formations, all of which have been intersected and identified during drilling. The mineralization within the Zhuchong Fe–Cu deposit is located in a deep-seated contact zone between a diorite intrusion and the Middle Triassic Yueshan Formation and contains lens and stratiform-like orebodies with forms controlled by the shape of the roof of the intrusion and the contact surface between intrusion and the surrounding country rocks. The orebodies within this deposit do not crop out (i.e., are concealed) and are deep-seated, being located at depths between 820 and 1350 m (Fig. 6).

The majority of the mineralization within the Zhuchong deposit is massive, banded and disseminated, with minor amounts of veined ore also present. The ore within the deposit generally contains magnetite, chalcopyrite, hematite and pyrrhotite with minor amounts of marcasite, bornite and sphalerite, all of which is hosted by a diopside, calcite, garnet, plagioclase, phlogopite, chlorite and actinolite gangue.

3. Exploration model

Before any prospectivity modeling can be undertaken it is important to define an exploration model that can be used to both inform the modeling process as well as providing insights during data interpretation. Because skarn-type Fe–Cu deposits dominate the Yueshan orefield, our exploration model represents a conceptual model that embodies the descriptive features of skarn-type mineralization as well as enabling the definition of exploration criteria for prospectivity modeling. The most important exploration criteria used within our exploration model are

Orogeny (Time)	Epoch	Lithostratigraphic Unit		Code	Thickness and Lithologic Composition
Indo-Sinian Orogeny (195 Ma)	Middle Jurassic	Luoling Formation		J_2l	2168 m, feldspar quartz sandstone, siltstone and silty shale, conglomerate at bottom
	Lower Jurassic	Moshan Formation		J_1m	624 m, feldspar sandstone, interlayers of silty shale and coal, conglomerate at bottom
	Upper Triassic	Lalijian Formation		T_3l	17~35 m, fine sandstone and siltstone with interlayers of carbonaceous shale and coal
	Middle Triassic	Tongtoujian Formation		T_2t	1735 m, siltstone, interlayers of sandy shale and interlens of fine sandstone
		Yueshan Formation	Upper	T_2y^2	43 m, siltstone, interlayered lens of marl in lower part
			Lower	T_2y^1	110 m, dolomite and limestone breccia
250 Ma	Lower Triassic	Nanlin ghu Formation		T_1n	>420 m, thin- to mid-thick limestone, with argillic bands in upper and lower
		Helongshan Formation		T_1h	42 m, argillic band-bearing limestone
		Yingkeng Formation		T_1y	60 m, limestone with interlayers of silt shale
	Upper Permian	Dalong Formation		P_2d	28~58 m, siliceous shale and argillo-calcareous shale, interlayers of limestone
		Longtan Foration		P_2l	58~73 m, fine sandstone, silt shale and shale, interlayers of coal
	Lower Permian	Gufeng Formation		P_1g	35~41 m, siliceous slate and siliceous shale
290 Ma		Qixia Formation		P_1q	218~246 m, chert-bearing bioclastic limestone and carbonaceous shale in lower
	Upper Carboniferous	Chuanshan Formation		C_3c	25 m, orbicular limestone and bioclastic limestone
	Middle Carboniferous	Huanglong Formation		C_2h	74~141 m, bioclastic limestone, dolomite with fine quartz conglomerate
	Upper Devonian	Wutong Formation		D_3w	29~94 m, quartz sandstone and silty shale
	Mid Silurian	Fentou Formation		S_2f	115 m, sandstone, siltstone and sandy shale
	Lower Silurian	Gaojiabian Formation		S_1g	776 m, graptolite-bearing black shale

Fig. 3. Stratigraphy of the Yueshan orefield (modified after Liu et al., 2010).

given below:

3.1. Sedimentary units

The skarn-type mineralization within the Yueshan orefield is associated with dolomite and limestone units that preferentially host mineralization in the study area. These middle Carboniferous to Middle Triassic rocks are littoral to neritic carbonates that are interbedded with bathyal facies sediments and alternate with marine to continental clastic sediments (Liu et al., 2011).

3.2. Intrusions

Numerous ~140 Ma diorite–quartz diorite–monzodiorite intrusions are located within the Yueshan orefield, including the Yueshan, Zongpu and Wuheng intrusions. The skarn-type deposits within the Yueshan orefield are closely associated with dioritic composition intrusions.

3.3. Structures

The Fe–Cu mineralization is preferentially located close to faults and is associated with domes, depressions and roof segments within the diorite intrusions as well as tongue shaped contact zones between Triassic sediments and diorite intrusions, all of which are used as exploration criteria in this study.

Previous research on computational simulations indicates that the orebodies within the Anqing deposit are mostly localized in high dilation zones as a result of incremental volumetric strain (Liu et al., 2011, 2012). The mechano-thermo-hydrological (MTH) processes that operate in these areas cause rocks to deform, dilate, and eventually fail. This in turn can induce incremental increases in volumetric strain that can facilitate the deposition of ores or the formation of space conducive to ore deposition (Liu et al., 2012). This indicates the importance of incorporating these regions in prospectivity modeling.

3.4. Geophysical characteristics

The carbonates in the study area have higher average densities than the diorite intrusions (~2.67×10^3 kg/m^3) in this region as well as the sandstone and siltstone units in this area (Table 1). This means that gravity geophysical data can be used to identify the majority of the mineralization-related rocks in the study area. In addition, the dioritic intrusions have average magnetic susceptibility values of ~4000×10^{-5} SI whereas the magnetite mineralization in this area

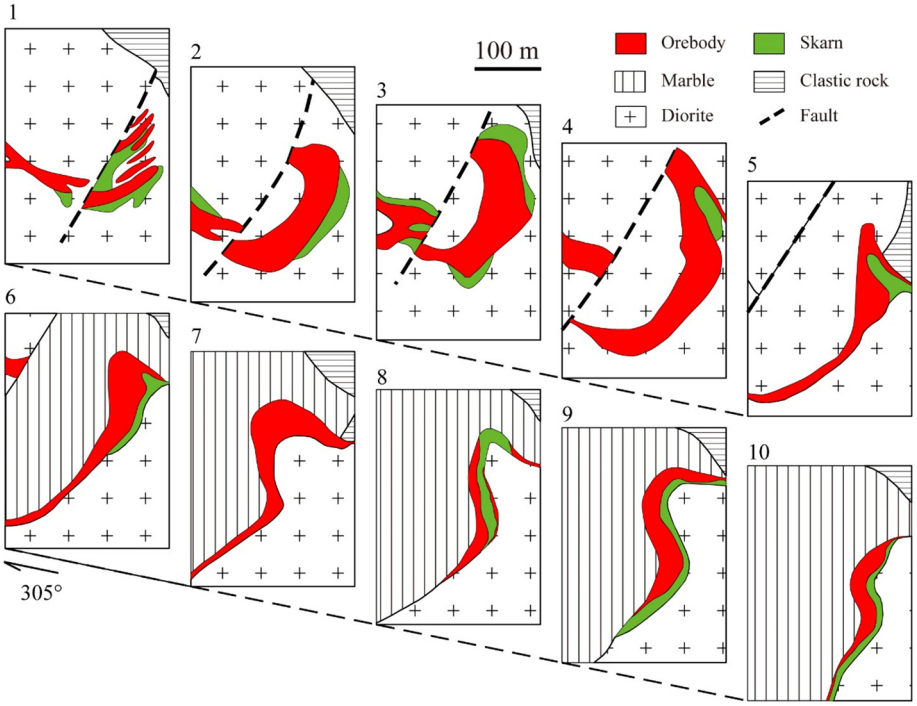

Fig. 4. Cross-sections through the Anqing Fe–Cu skarn deposit where numbers on individual cross-sections represent successive different profiles that show variations in the shapes of the orebodies within the deposit, associated intrusions, and the surrounding country rocks (Zhou et al., 2007).

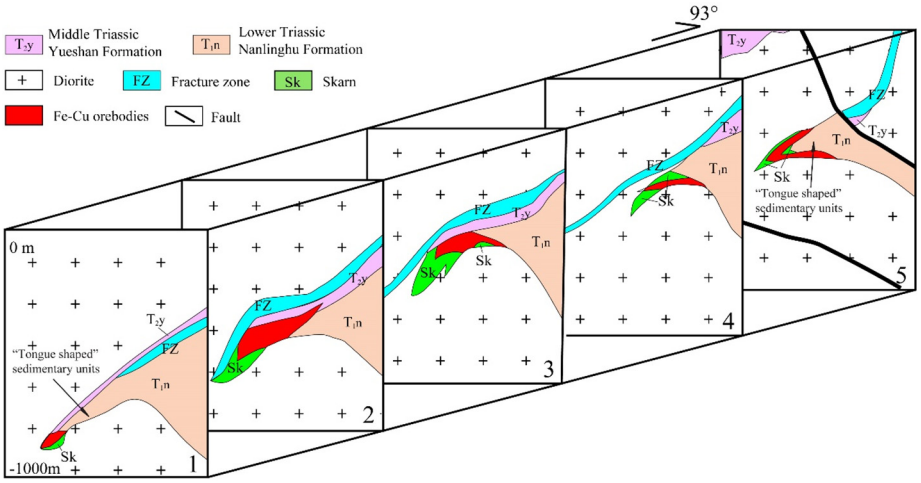

Fig. 5. Cross-sections through the Matoushan Fe–Cu skarn deposit; numbers on individual cross-sections represent successive different profiles showing the variations in the shapes of orebodies, intrusions and surrounding country rocks.

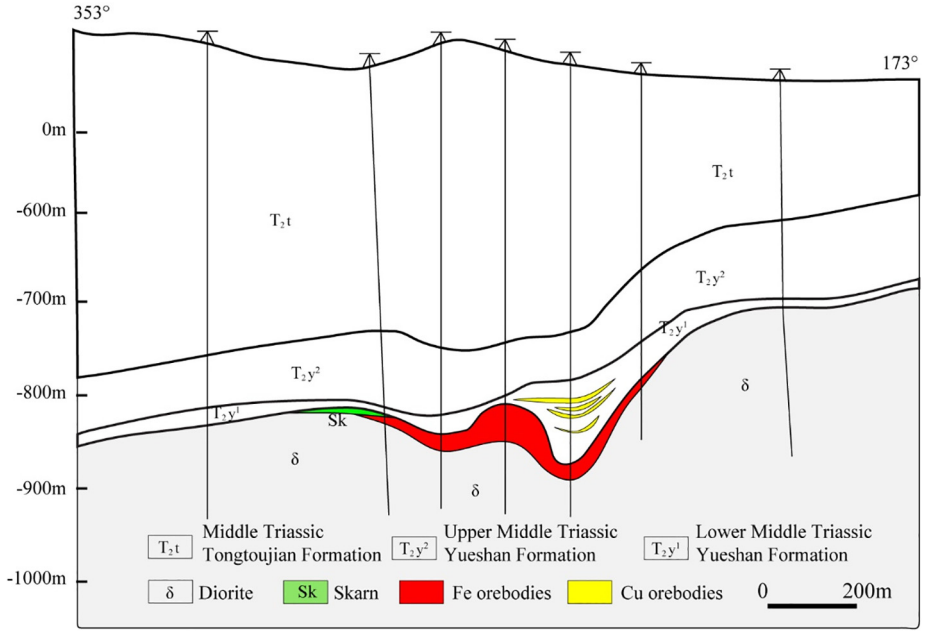

Fig. 6. Cross-section through the Zhuchong Fe–Cu deposit showing the shape of the orebodies and their relationship to the shape of the roof of the intrusion and the contact zone between the intrusion and the surrounding country rocks.

Table 1
Average densities, magnetic susceptibilities and electrical resistivities of different lithologies in the Yueshan orefield.

Lithology	Average density (g/cm^3)	Average magnetic susceptibility (10^{-5}SI)	Electrical resistivity (average) (Ωm)
Sandstone	2.62	0	21-5402 (643)
Siltstone	2.65	0	506-11863 (3562)
Shale	2.69	0	10(Coal) -1000 (820)
Carbonate	2.73	0	998-10825 (5522)
Diorite	2.67	4.02×10^3	314-19480 (9064)
Fe-Cu Orebodies	4.15	8.10×10^4	< 1

has an average magnetic susceptibility value of around 80000×10^{-5} SI. This means that both diorite intrusions and shallow magnetite mineralization can be magnetically detected and potentially discriminated between in the study area. However, the depth of the intrusions and mineralization also plays a role in that deep-seated diorite intrusions may be associated with weakly magnetic anomalies at the surface, and deep-seated magnetite mineralization is difficult to detect in this region as a result of the magnetic susceptibility of the diorite intrusions. Therefore, deep-seated Zhuchong Fe–Cu deposit has not been discovered until 2012 by the use of controlled source audiofrequency magnetotelluric (CSAMT) data to identify geological structures and low resistivity anomalies at depth in the study area.

4. Methodology and results

The workflow and methods used in 3D mineral prospectivity modeling have been discussed in detail in a number of recent studies (e.g. Sprague et al., 2006; Mao et al., 2011; Xiao et al., 2012; Yuan et al., 2014a,b) and as such are summarized here. Initial joint geophysical inversion and forwarding modeling and 3D geological modeling approaches are used to combine available geological and geophysical data within a 3D geological model of the study area. This initial step is

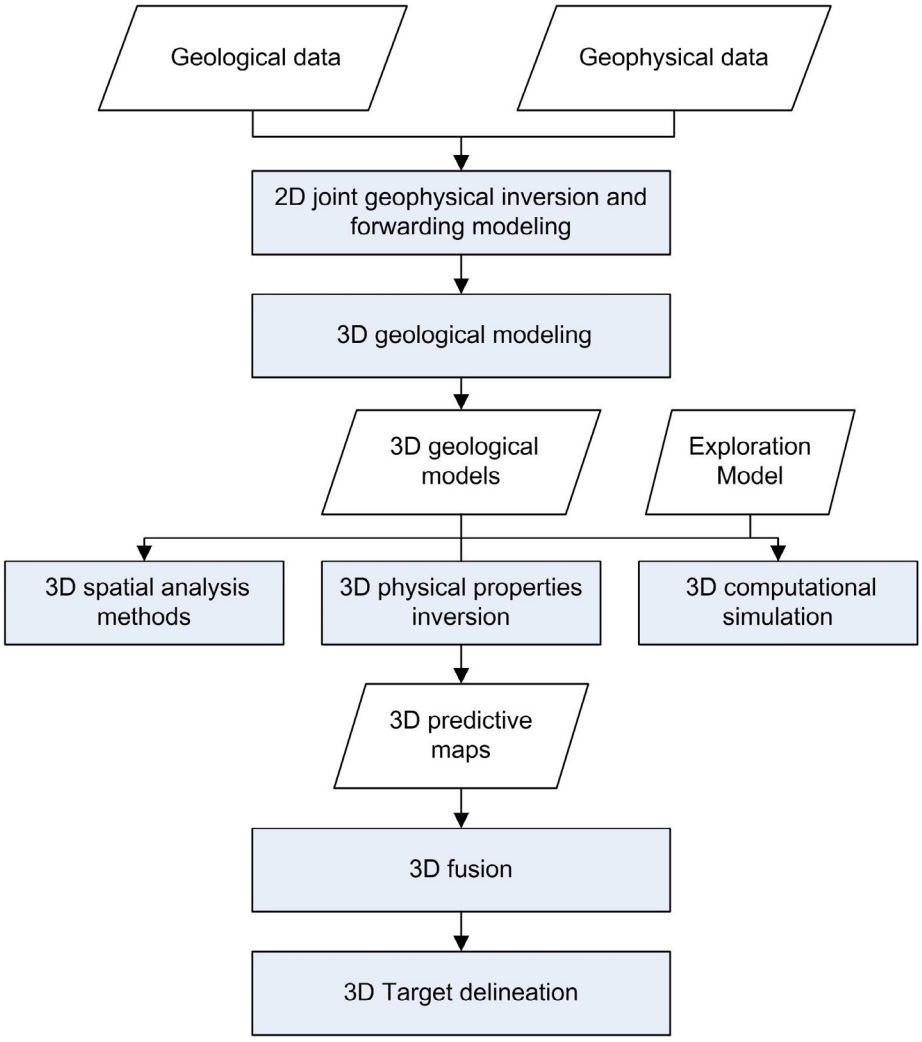

Fig. 7. Workflow of the 3D mineral prospectivity modeling approach used during this study.

followed by the definition of an exploration model that is used with training point data to yield a 3D prospectivity model and finally a quantitative 3D predictive map. These approaches generally include both 3D spatial analysis and 3D geophysical inversion methods. This study presents a 3D computational simulation based approach that allows the generation of new quantitative 3D predictive maps from 3D data and geological models, improving the efficiency and accuracy of 3D mineral prospectivity modeling. This allows 3D data fusion modeling based on approaches such as weights of evidence or logistic regression to be used to integrate all of the 3D predictive maps constructed for the study area by analyzing the spatial relationships between these 3D predictive maps and the known extent of mineralization. This allows the delineation and identification of exploration targets in 3D and the overall process involved is summarized in the flowchart shown in Fig. 7.

Some 2.08 million 50 × 50 × 50 m cubic blocks were used to define the 3D volume space of the study area, with the dimensions of the cubic blocks representing the average thickness of the skarn orebodies that define the skarn-type Anqing and Zhuchong Fe–Cu deposits. These cubic blocks are used for 3D spatial analysis to generate 3D predictive maps and 3D data fusion to map the mineral prospectivity of Yueshan orefield.

4.1. 3D geological modeling

The 3D mineral prospectivity modeling undertaken during this study is based on 3D geological models that form the basis of all of the 3D predictive maps generated during this. This approach to the 3D geological modeling was outlined in detail by Malehmir et al. (2009) and Lü et al. (2012) and involves five steps, namely (1) defining the 3D limits of the model area, (2) constructing a series of 2D cross-sections over the model area, (3) integration and interpretation of these 2D geological cross-sections with surface geology and borehole data, (4) geophysical forward modeling of the 2D cross-sections, and (5) final data integration and 3D visualization.

This study used seven N-W cross-sections at 2 km intervals (Fig. 2) through the Yueshan orefield to delineate geological contacts and structures at depth. The geological data used in the 3D geological modeling undertaken during this study included geological maps and more than 100 drillholes (maximum depth of 1556.35 m). These cross-sections also incorporate geophysical forward modeling and the interpretation and integration of gravity, magnetic and CSAMT data with the initial 2D cross-sections to yield final 2D cross-sections that are consistent with geological and drillhole constraints (Fig. 8). It should be noted that some of the sections of faults interpreted to represent the boundaries of different geological units during geophysical forward modeling are used in the 3D geological modeling undertaken during this study. The predictive information represented by these faults is shown as the contact surface of the favorable unit during this 3D prospectivity modelling. However, the other parts of faults identified during this modeling that do not have any control on the morphology of the units in the study area are relatively small and also cannot be

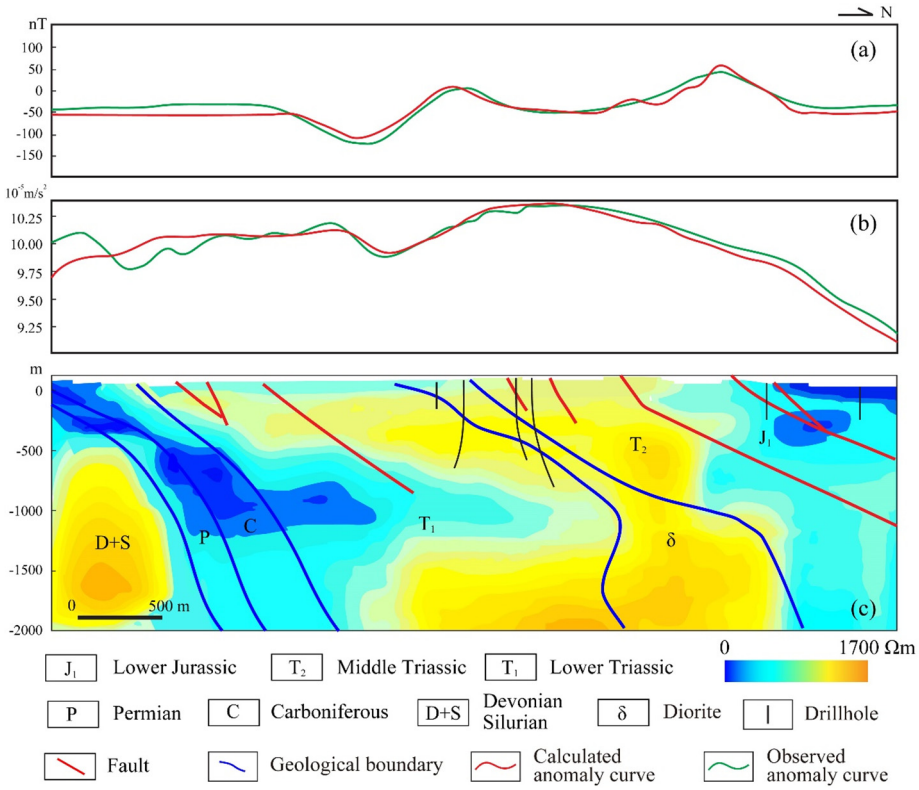

Fig. 8. Selected cross-sections showing the joint geophysical modeling undertaken during this study, including (a) observed and calculated magnetic anomalies generated during forward modeling, (b) observed and calculated gravity anomalies generated during forward modeling, and (c) the CSAMT inversion and the joint geophysical model.

accurately delineated using geophysical forward modelling. As such, these small sections of the faults identified by geophysical forward modeling were not used during the 3D geological modeling undertaken during this study.

Implicit 3D geological modeling based on potential field interpolation enabled the automatic integration of multi-source data, including 2D geological maps and cross-sections and 2D geophysical data and maps and cross-sections generated by joint geophysical inversion and forward modeling with a priori structural information and the geological knowledge of an area (Calcagno et al., 2008; Jessell, 2001). Therefore, this study uses an implicit 3D geological modeling approach that employs Geomodeller™ software to incorporate data from geological maps and cross-sections with the geophysical models and drillhole data mentioned above (Fig. 9). It should be noted that some of the drillholes located close to individual cross-sections have been used to constrain 2D joint geophysical models, with other drillholes that lie between individual cross-sections also being used in the 3D geological modeling presented in this study (Fig. 9c).

4.2. 3D predictive map generation

4.2.1. 3D computational simulations

Computational simulation methods have been widely used during investigations into the processes involved in the generation of complex magmato-hydrothermal (e.g. skarn-type) mineral deposits, and recent advances in this area include the 3D modeling of these systems (Liu et al., 2012; Murphy et al., 2008; Ord et al., 2002). Computational simulation methods can provide insights into the dynamic and genetic relationships between igneous intrusions and skarn-type mineralization (as well as other classes of mineral deposit) using approaches such as coupled simulating deformation and the modeling of heat transfer and fluid flow during mineralization and the cooling of ore-related intrusions.

Magmato-hydrothermal mineral deposits such as skarns form as a result of coupled MTH processes; for example, deformation in an area can influence hydrothermal fluid pressures, whereas changes in effective stress as a result of changes in fluid pressures can result in deformation. In addition, temperature variations can result in thermal

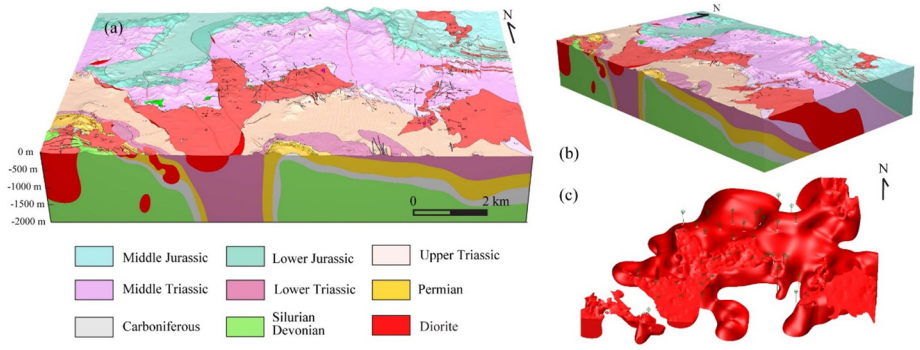

Fig. 9. 3D geological model of the Yueshan orefield generated during this study, including (a) front view of the 3D geological model, (b) oblique view of the 3D geological model, and (c) 3D model for the diorite intrusion in this area incorporating drillhole data as further constraints.

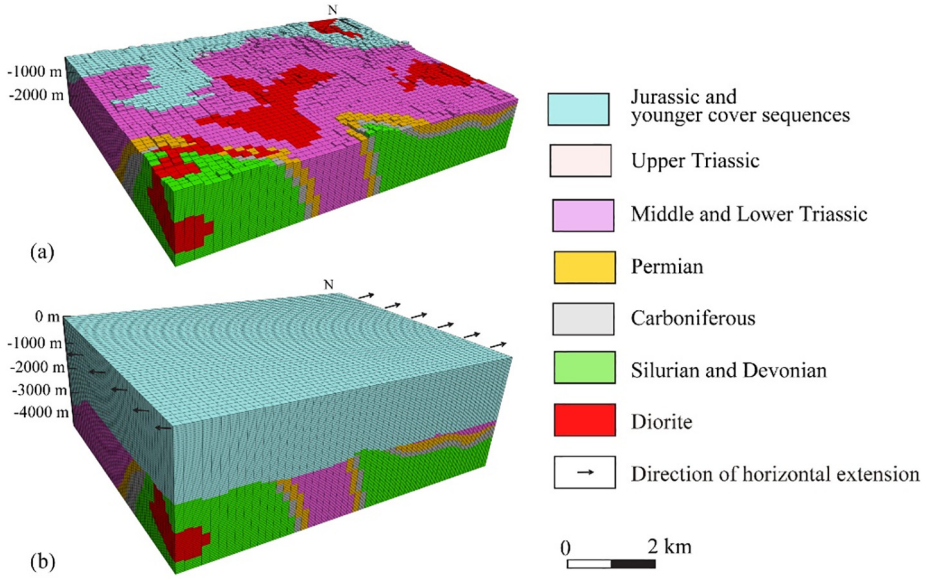

Fig. 10. 3D geological models used during 3D computational simulations (a) without 2500 m Jurassic cover and (b) covered by 2500 m of Jurassic sediments.

expansion and the development of temperature gradients can trigger the movement of hydrothermal fluids that can in turn further transfer heat energy within the system by convection (Ord et al., 2012a,b; Zhao et al., 2008).

Here, we use computational simulation methods to simulate MTH processes during the syn-extensional cooling of the intrusion in order to identify concealed high dilation zones that are known to preferentially host magmato-hydrothermal mineralization (Liu et al., 2011). We define the intrusion and the surrounding wall rocks as Mohr–Coulomb materials where the governing equations used for simulating MTH processes are described as follows (FLAC3D User's Guide, 2012):

$$q^W = -k\nabla(P - \rho_w g \cdot x) \tag{1}$$

Eq. (1) is Darcy's law describing fluid flow, where q^W is fluid specific discharge, k is the fluid mobility coefficient, P is the pressure of the pore fluid, ρ_w is fluid density, and g is gravitational acceleration.

$$q^T = -k^T \nabla T \tag{2}$$

Eq. (2) is Fourier's law describing heat conduction, where q^T is heat flux, k^T is the effective thermal conductivity, and T is temperature.

$$\frac{\partial \zeta}{\partial t} = -q_{i,i} + q_v^W \tag{3}$$

Eq. (3) describes the conservation of mass, where ζ is the variation of fluid content, q_i is the fluid specific-discharge vector in the x_i direction, and q_v^w is the volumetric fluid source.

$$C^T \frac{\partial T}{\partial t} + \nabla q^T + \rho_0 c_w q^W \cdot \nabla T - q_v^T = 0 \tag{4}$$

Eq. (4) describes the energy balance for convective-diffusive heat transport, where C^T is the effective specific heat, T is temperature, q^T is heat flux, ρ_0 and C_w are the reference density and the specific heat of the fluid, respectively, and q_v^T is the volumetric fluid source.

$$\rho \frac{d\upsilon_i}{dt} = \sigma_{ij,j} + \rho g_i \tag{5}$$

Eq. (5) describes the conservation of momentum, where$\upsilon_i$is the velocity component in the x_i direction, ρ is the bulk density of the porous medium, σ_{ij} is the stress tensor of the solid, and g_i is the component of gravitational acceleration in the x_i direction.

$$\frac{\partial \varepsilon_{ij}}{\partial t} = \alpha_t \frac{\partial T}{\partial t} \delta_{ij} \tag{6}$$

$$\frac{\partial P}{\partial t} = M\left(\frac{\partial \zeta}{\partial t} - \alpha \frac{\partial \varepsilon}{\partial t} + \beta \frac{\partial T}{\partial t}\right) \tag{7}$$

Finally, Eqs. (6) and (7) describe the coupled MTH constitutive relation, where ε_{ij} is the thermal strain tensor, T is temperature, α_t is the coefficient of linear thermal expansion, δ_{ij} is the Kronecker delta, ζ is the variation in fluid content, M is the Biot modulus, α is the Biot coefficient, ε is the volumetric strain, and β is the volumetric thermal expansion of the porous matrix.

This study uses FLAC3D, a 3D finite-difference software, to solve the governing equations used for simulating MTH processes within discrete 3D geological models (Itasca Consulting Group, 2002). The 3D computational simulations undertaken during this study were split into three steps as follows:

(1) Construction of a 3D geological model for 3D computational simulations
The fact that implicit 3D geological modeling is based on discrete 3D cells means that this approach can directly provide discrete 3D geological models for use with the FLAC3D software. The 3D geological models (Fig. 9) constructed during this study were exported as hexahedral models although the computational capability limits meant that the hexahedron cells were limited to a size of 260 × 200 × 50 m to accelerate computation time, a cell size that is larger than the cubic blocks used during 3D prospectivity modeling (Fig. 10a).
The stratigraphy of the Yueshan orefield (Fig. 3) indicates that up to 2.5 km of sandstone was originally present above the outcropping units in this region at the time of mineral deposit genesis in this area. Previous research indicates that the ore-forming fluids that generated the skarn-type Anqing deposit (currently located at depths of −280 to −580 m) were under pressures of around 8×10^7 Pa (Zhou et al., 2007). Assuming these ore-forming fluids were under lithostatic pressure indicates that these orebodies were originally located some −3000 m below the surface. As such, we reconstructed this in the geological model used for 3D computational simulations by adding some 2500 m of Jurassic sedimentary units to the top of the model (Fig. 10b).
(2) Setting of properties and boundary conditions
The previous research undertaken on the Yueshan orefield (Liu et al., 2012) provided the hydrological, mechanical and thermal properties of the units in the model used during this study (Fig. 3).

The initial temperature of the top surface is set at 25 °C and is kept constant with an initial temperature gradient of 20 °C/km for the sedimentary section and an initial intrusion temperature of 700 °C. The initial pore pressure of the sedimentary rocks is set to hydrostatic conditions, whereas the initial pore pressure of the intrusion is set to be near lithostatic.

The timing of formation of the diorite intrusion and associated mineralization within the Yueshan orefield was associated with a change from compressional to extensional tectonic regime in the lower Yangtze River region (Dong and Qiu, 1993; Mao et al., 2006a,b). As such, our models are set to horizontally extend with a symmetrical boundary velocity of $2.4 \times 10^{-10}\,ms^{-1}$ at both sides parallel to the E–W direction of the model to represent this tectonic extension (Liu et al., 2012; Fig. 10b).

(3) 3D computational simulation

The rock properties and boundary conditions outlined above enabled the development of a geological model (Fig. 10b) that simulates the syn-extensional cooling evolution of the Yueshan intrusion under controlled time-step conditions. Previous research indicates that the orebodies within the Anqing deposit are mostly located in high dilation zones as a result of incremental volumetric strain, a process that can facilitate the deposition of ores or the formation of space conducive to ore formation (Liu et al., 2012). This means that incremental increases in volumetric strain represent an exploration criterion that can be used in 3D prospectivity modeling.

The simulation ran for a thousand years and generated the major orebodies within the Anqing and Yueshan deposit, all of which are located at different depths within high dilation zones (i.e., high incremental volumetric strain increase zones) along the contact zone between the intrusion and the surrounding Triassic country rocks (Fig. 11). Simulation result not only clearly delineates the relationship between high dilation zones and known mineral deposits but also highlight some hitherto unknown high dilation zones within the margin of the intrusion (Fig. 12a). This means that this simulation-based approach could be a useful tool in terms of identifying areas for future exploration. In addition, this simulation highlights numerous high dilation zones in the study area, meaning that the results of this simulation results can be combined with other predictive maps to reduce exploration uncertainty in this region.

3D distance fields (or 3D buffers) can allow the identification of spatial relationships between mineralization and individual mineral exploration criteria as well as providing 3D predictive maps for 3D data fusion and targeting, but also can decrease the uncertainties caused by inaccuracies within 3D geological models, theoretical limitations and the precision of 3D computational simulations, 3D spatial analysis and 3D physical property inversions. Here, we use a 3D signed Euclidean distance transformation method that can enable significant increases in computational efficiency (Lin and Wang, 2003; Jones et al., 2006; Li et al., 2016) to initially calculate 3D distance fields for the location of high dilation zones. The 3D distance fields for the remaining exploration criteria were then generated using 3D spatial analysis, with later inversion of the 3D physical properties in the study area.

4.2.2. 3D spatial analysis

The orebodies that constitute mineral deposits such as skarns are always controlled by the spatial distribution and morphology of individual geological bodies or structures that are often termed mineral exploration criteria. Here, we use 3D spatial analysis methods including 3D mathematical morphology and Gaussian curvature calculation method to define and extract the mineral exploration criteria described in Section 3 (and based on the exploration model outlined above) from the 3D geological model constructed during this study. As outlined above, the 3D spatial analysis methods used in this paper use 2.08 million 50 × 50 × 50 m cubic blocks to define the 3D spatial space of the study area, with the dimensions of these cubic blocks representing the average thickness of the skarn orebodies within the skarn-type Anqing and Zhuchong Fe–Cu deposits.

(1) Sedimentary units

The exploration model defined above indicates that the majority of skarn-type mineralization within the Yueshan orefield is hosted close to or along the contacts of dolomitic and calcareous sedimentary units, including a series of middle Carboniferous to Middle Triassic formations. The modeling undertaken during this study defined 3D geological models for each of these Carboniferous to

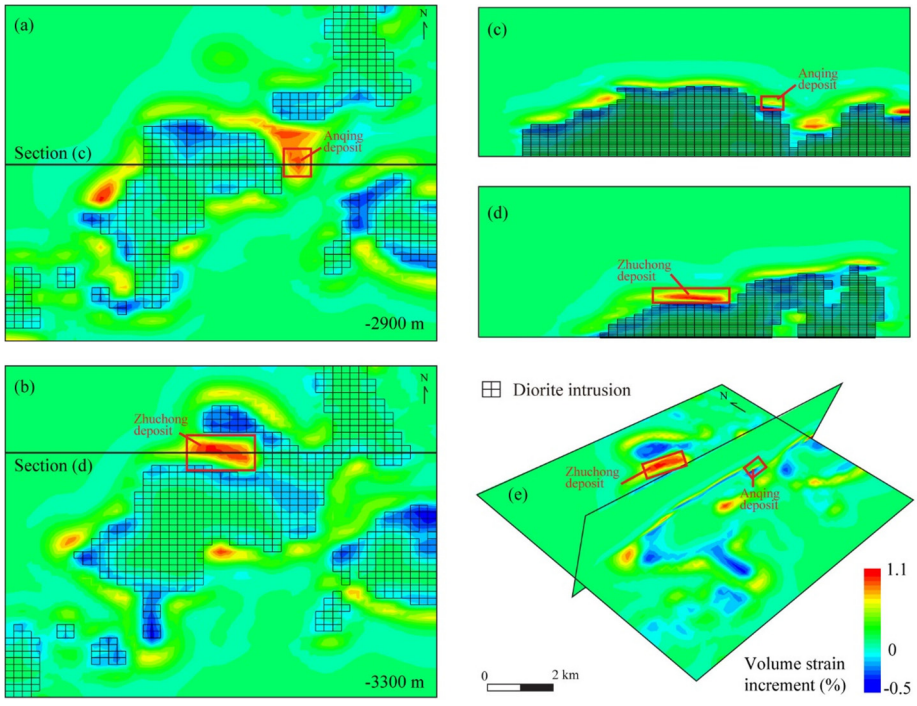

Fig. 11. Changes in incremental volume strain after 3D computational simulation shown on (a) plan view at a depth of −2900 m (equal to −400 m at the present-day), (b) plan view at −3300 m (equal to −800 m at the present-day), (c) cross-section across the Anqing deposit, (d) cross-section across the Zhuchong deposit, and (e) a 3D overlay of cross-section and plan views.

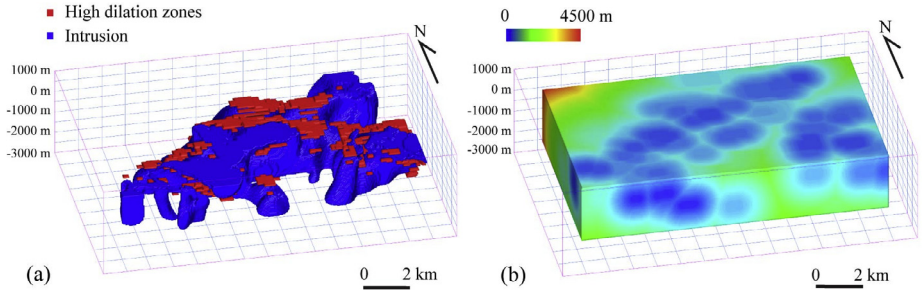

Fig. 12. (a) Location of blocks within high dilation zones in the vicinity of the margins of the diorite intrusion and (b) 3D model showing variations in spatial proximity to high dilation zones.

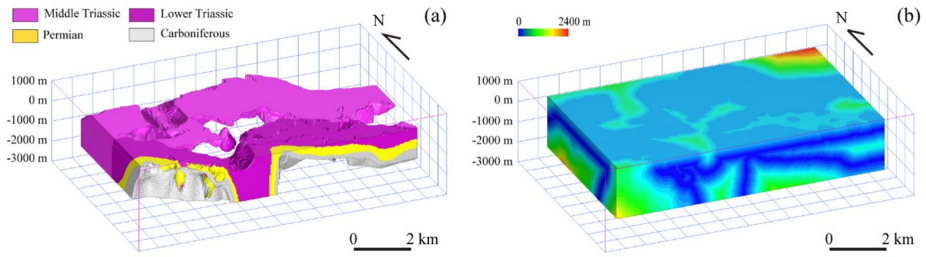

Fig. 13. (a) 3D model of the Carboniferous to Middle Triassic sedimentary units in the study area and (b) 3D model showing variations in proximity to the contact surface of these sedimentary units.

Middle Triassic sedimentary units and extracted contact surfaces for each individual sedimentary unit (Fig. 13a). These surfaces were then used to determine the distance between each contact surface and every cubic block in the study area (Fig. 13b).

(2) Intrusions

Skarn-type mineralization is closely associated with diorite intrusions that were intruded into the sediments in the study area, meaning that the proximity to the diorite-sedimentary contact is another exploration criterion that needs to be modeled. This involved the initial extraction of the contact surface of the dioritic intrusion using the same approach used for the sedimentary units (Fig. 14a) before calculating the distance between this contact surface and every cubic block in the study area (Fig. 14b).

(3) Faults

Fault sets can provide preferential pathways for the movement of magmas as well as the migration of ore-forming hydrothermal fluids. In this study, only a small part of faults can be interpreted based on the cross-sections, but more potential faults can be inferred based on ground gravity geophysical data. It should be noted that these faults have been vertically extended to depth to enable the construction of a 3D fault model independently for the study area (Fig. 15a). This vertical extension is used because the available ground gravity data makes it very difficult to infer the actual attitude and extension of these potential faults. However, we also consider including rather than excluding these faults is a better approach as they may provide some information that is useful during 3D prospectivity modeling, with the possible improvement of these initial 3D fault models using future geological and geophysical work.

The vertically extrapolated faults are surrounded by calculated 3D distance fields (i.e., buffers) in our model (Fig. 15b). These 3D distance field represents an envelope around the fault that indicates areas that may have been affected by mineralization-related hydrothermal or magmatic activity. In addition, compared with the 3D fault models, these buffers envelope larger areas in our modeling which may reduce the uncertainty associated with the vertical extrapolations of these faults, compensating for a lack of knowledge of the unknown dips of these faults.

(4) Doming and depressions within the contact between the diorite intrusion and the surrounding country rock.

The exploration model described above indicates that both domes and depressions within the contact surface of the diorite intrusion are favorable locations for mineralization. This is exemplified by the fact that the majority of mineralization within the known Zhuchong Fe–Cu deposit is located within domes and depressions in the diorite intrusion. The results of our 3D computational simulations also indicate that some high dilation zones are located in domes and depressions of the contact between the diorite intrusion and the surrounding country rock, again indicating that these locations are favorable for the focusing of fluid flow and mineralization. The location of domes and depressions within the diorite intrusion contacts were extracted (Fig. 16) by measuring the geometrical characteristics of surfaces using a Gaussian curvature approach (K_{CG}; Li et al., 2015):

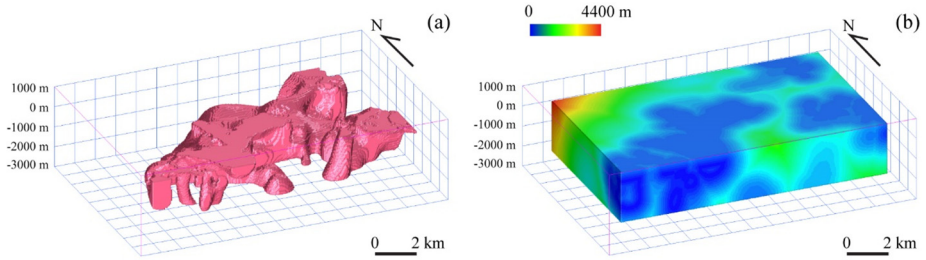

Fig. 14. (a) 3D model of the diorite intrusion and (b) 3D model showing variations in proximity to the contact surface of diorite intrusion within the study area.

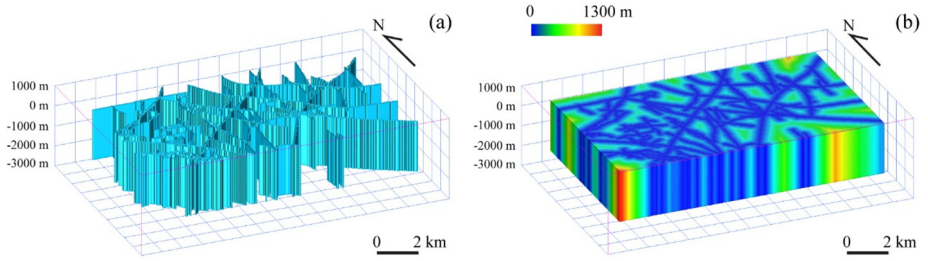

Fig. 15. (a) 3D model of faults within the study area faults and (b) 3D model showing variations in the proximity to faults within the study area.

$$K_{CG} = K_1 K_2 \tag{8}$$

where K_1 and K_2 are the maximum and minimum or principal curvatures. Areas with K_{CG} values > 0 are indicative of surfaces bending away from the tangent plane in all tangent directions (Pressley, 2010) and represent areas of doming or depressions.

(5) Tongue shaped sedimentary units.
The orebodies within the Anqing and Matoushan Fe-Cu deposits are always located in tongue-shaped zones within sedimentary units that are surrounded by the dioritic intrusion and protrude away from the main sedimentary units (Fig. 5). Typical 3D mathematical morphology methods that can be used to identify areas with these morphologies include trend, convex–concave and undulation analytical methods (Mao et al., 2016). Here we use a convex–concave analysis method to extract the locations of tongue shaped Carboniferous to Middle Triassic sedimentary units (Fig. 17) that are related to mineralization (Fig. 18) as follows:

$$D(A) = A \cap \psi_{co}(\bar{A}, B) \tag{9}$$

where $D(A)$ is the tongue shaped sedimentary unit, A is the sedimentary unit in question, B is a structuring element, such as a isotropic sphere structuring element and $\psi_{co}(A, B)$ represents the results of the filtering of the opening and closing operators combined together, which are in turn defined as:

$$\psi_{co}(A, B) = A \bullet B \circ B \tag{10}$$

where ∘ and • are basic morphological filters with opening denoted by ∘, and closing denoted by • (Serra, 1986; Mao et al., 2016).

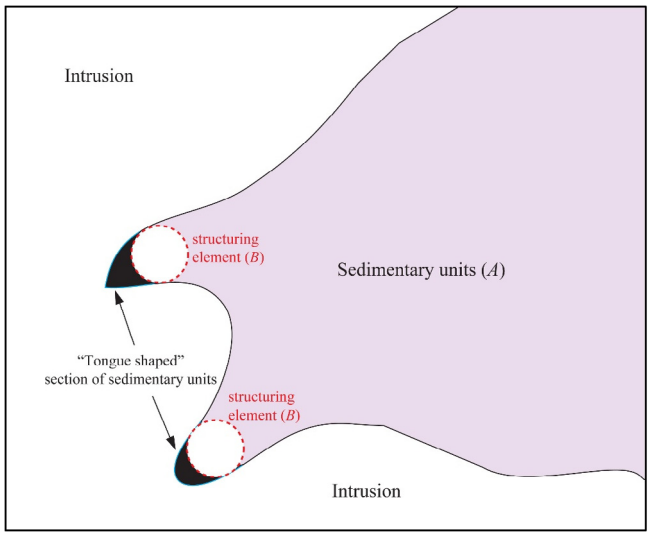

Fig. 17. Schematic plan view showing the location of tongue shaped section of sedimentary units extracted using the 3D mathematical morphology method outlined in the main text.

4.2.3. 3D physical property inversion

Li and Oldenburg (1996, 1998) outlined a geologically-constrained 3D property inversion algorithm for the prediction of geology beneath cover, an approach that allows the representation of any complicated geological bodies at depth as well as identifying areas containing prospective host rocks, structures, alteration and mineralization beneath the surface. This 3D property inversion algorithm uses a model objective function that includes a term that measures the difference between the recovered model and a reference model, and how the difference between recovered and reference models varies between cell in each of three orthogonal directions (Williams, 2008). The model objective function is as follows:

$$\begin{aligned}\varphi_m m = {} & a_s \int_V w_s [w_r(z)(m - m_{ref})]^2 dV + \\ & a_x \int_V w_x \left[\frac{\partial (w_r(z)(m - m_{ref}))}{\partial x}\right]^2 dV + \\ & a_y \int_V w_y \left[\frac{\partial (w_r(z)(m - m_{ref}))}{\partial y}\right]^2 dV + \\ & a_z \int_V w_z \left[\frac{\partial (w_r(z)(m - m_{ref}))}{\partial z}\right]^2 dV +\end{aligned} \tag{11}$$

where m is the recovered model and m_{ref} is the reference model. The first integral component measures the smallness and last three integral components measure the smoothness of the difference between m and

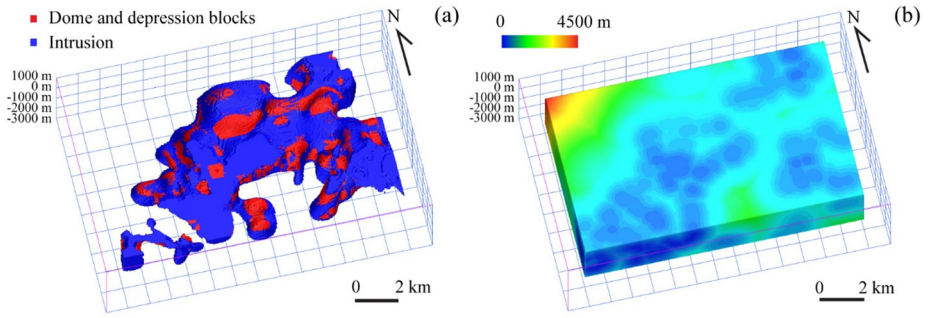

Fig. 16. (a) Location of blocks within domes and depressions in the diorite intrusion contact surface and (b) 3D model showing variations in spatial proximity to dome and depression zones within the diorite intrusion contact.

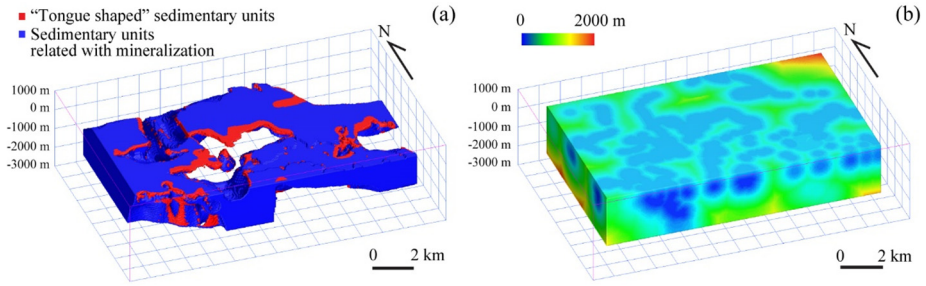

Fig. 18. (a) Location of blocks within tongue shaped sedimentary units and (b) 3D model showing variations in proximity to these blocks within tongue shaped sedimentary units.

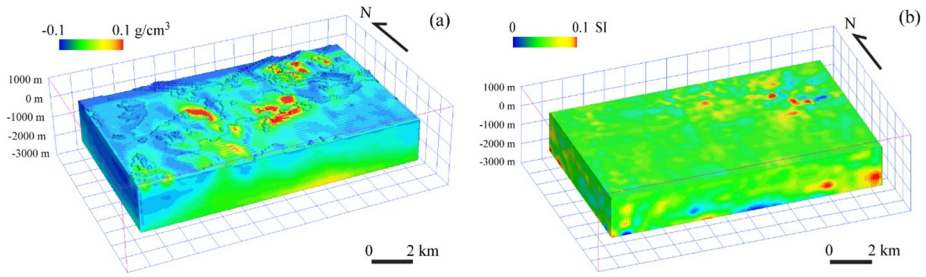

Fig. 19. 3D property inversions of (a) density and (b) magnetic susceptibility for the study area.

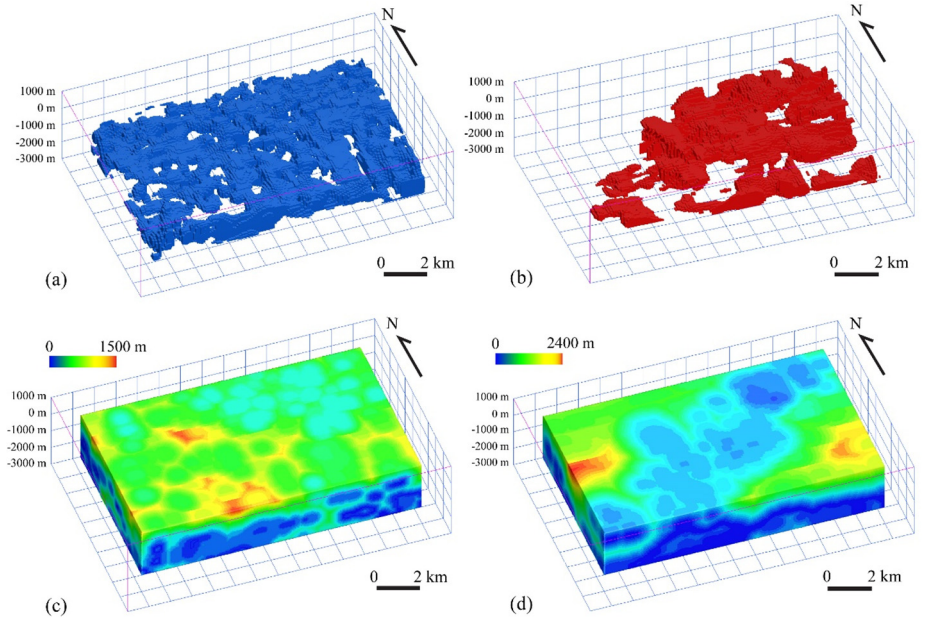

Fig. 20. 3D models showing the location of (a) high density and (b) high magnetic susceptibility geological bodies and variations in proximity to blocks within (c) high density and (d) high magnetic susceptibility geological body contact surfaces.

m_{ref}, α_s, α_x, α_y, and α_z are used to balance the contributions of the smallness and smoothness components, w_s, w_x, w_y, and w_z are weighting functions and are spatially dependent, and the function $w_r(z)$ is a depth weighting to counteract the decay of the potential field response with distance from the source (Williams, 2008).

The geologically-constrained 3D property inversion algorithm mentioned above was used to inversely calculate the density and susceptibility of individual cells within the study area. The gravity data used for inversion in this paper was measured on a 200 × 200 m grid, with magnetic data measured on a 100 × 100 m grid and a reference model built using geological mapping and physical property information. A satisfactory fit to the observed data was achieved after a number of iterations (Fig. 19). As mentioned in Section 3 and Table 1, high density (> 2.67 g/cm^3 density) cells most likely represent mineralization-related carbonate, dolomite, limestone, marble or magnetite units and high magnetic susceptibility (> 4000 × 10^{-5} SI) cells most likely correspond to the diorite intrusion and magnetite. Therefore, this means that the high density and magnetic susceptibility cells related to Fe–Cu mineralization can be further extracted in 3D using 3D geophysical inversion models respectively (Fig. 20).

4.3. 3D data fusion and mineral prospectivity mapping

Data-driven models have a number of advantages over knowledge-driven models during brownfield exploration, the most important of which is the fact that data-driven models can objectively identify and

Table 2
Parameters used in the 3D computational simulation model (modified after Liu et al., 2012).

Model unit	Density (kg/m^3)	Bulk modulus (10^{10} Pa)	Shear modulus (10^{10} Pa)	Tensile Strength (10^6 Pa)	Cohesion (10^{10} Pa)	Friction Angle (°)	Dilation angle (°)	Permeability (10^{-18} m^2)	Porosity	Thermal conductivity (W.m^{-1}k^{-1})
Jurassic Formation and Younger cover sequences	2520	2.80	0.9	1.8	3.8	25	3	25.0	0.25	1.8
Upper Triassic Formation	2560	3.20	1.92	2.2	4.0	32	4	28.0	0.22	2.2
Middle and Lower Triassic Formation	2620	4.80	2.6	3.2	5.8	38	18	4.2	0.18	3.2
Permian Formation	2630	3.50	2.1	2.3	4.5	28	21	19.0	0.19	2.3
Carboniferous Formation	2615	2.20	1.2	1.8	3.2	10	5	8.6	0.15	4.5
Silurian and Devonian Formation	2560	3.20	1.92	2.2	4.0	32	4	28.0	0.22	2.2
Diorite Intrusion	2600	2.95	1.97	2.2	3.8	25	8	8.5	0.12	2.0

quantify spatial relationships between data inputs and mineralization. In this paper, logistic regression (Chung and Agterberg, 1980) and weights of evidence (Bonham-Carter et al., 1989) approaches are used to integrate all of the 3D predictive maps and highlight exploration targets at depth; both of these approaches have recently been used in 3D prospectivity modeling (Payne et al., 2015; Yuan et al., 2014a,b; Li et al., 2015).

(1) Logistic regression model.
Logistic regression modeling generates mineral prospectivity maps by integrating continuous and bivariate predictive maps but does not use assumptions about the probability distribution of the independent predictive variables and the conditional independence of the predictive maps (Carranza and Hale, 2001; Porwal and Kreuzer, 2010). All of this can be expressed as follows:

$$\pi(d) = \frac{e^{\alpha+\beta_i x_i}}{1 + e^{\alpha+\beta_i x_i}} \tag{12}$$

where $\pi(d)$ is the probability of a mineralized occurrence, x_i is the ith (i = 1 to N) predictive map, α is a constant, and β_i is the regression coefficient for x_i.

(2) Weights of evidence.
Weights of evidence modeling is a bivariate statistical approach that is based on Bayes' theory of conditional probability and quantifies the relationship between the mapped distribution of a given dataset and training data, which in this case are areas of known mineralization. This approach combines a 3D geological space incorporating d given blocks containing mineralization and e_1, e_2, …, e_n values representing the different evidential datasets during modeling, yielding:

$$W_j^+ = ln\frac{P(e_j|d)}{P(e_j|\neg d)} \tag{13}$$

$$W_j^- = \ln\frac{P(\neg e_j|d)}{P(\neg e_j|\neg d)} \tag{14}$$

where W_j^+ is a positive weighting that indicates a positive spatial association between the evidence in a block (i.e. the 3D predictive maps mentioned above) and the presence of mineralization (i.e. the training data mentioned above) and W_j^- is a negative weight that indicates a negative spatial association between the evidence in a block and mineralization.

Posterior probability odds can be derived using:

$$P(d|e_1^k \cap e_2^k \cap \ldots \cap e_n^k) = \frac{O(d|e_1^k \cap e_2^k \cap \ldots \cap e_n^k)}{1 + O(d|e_1^k \cap e_2^k \cap \ldots e_n^k)} \tag{15}$$

where the odds *"O"* can be calculated based on the weights of evidence outlined above.

In order to demonstrate the influence of the 3D computational simulation (i.e., the location of high dilation zones) on this 3D prospectivity modeling, all of the 3D predictive maps described above (predictive Dataset A) were used to model the prospectivity of skarn-type Fe–Cu mineralization within the Yueshan orefield. Another additional predictive dataset (predictive Dataset B) was constructed, including all of the 3D predictive maps barring the results of the 3D computational simulation. The modeling of both Dataset A and B used the known locations of Fe–Cu skarn-type mineralization within the Anqing and Zhuchong deposits as training data to measure spatial or genetic associations between the predictive maps based on the data outlined above and the locations of areas of known mineralization. The training data representing areas of known mineralization were extracted using the cut-off grades (TFe > 25%) for the Zhuchong and Anqing deposit and are based on the results of 3D inverse distance weighting interpolation of drillhole sample grades.

Weights of evidence modeling has a number of advantages over

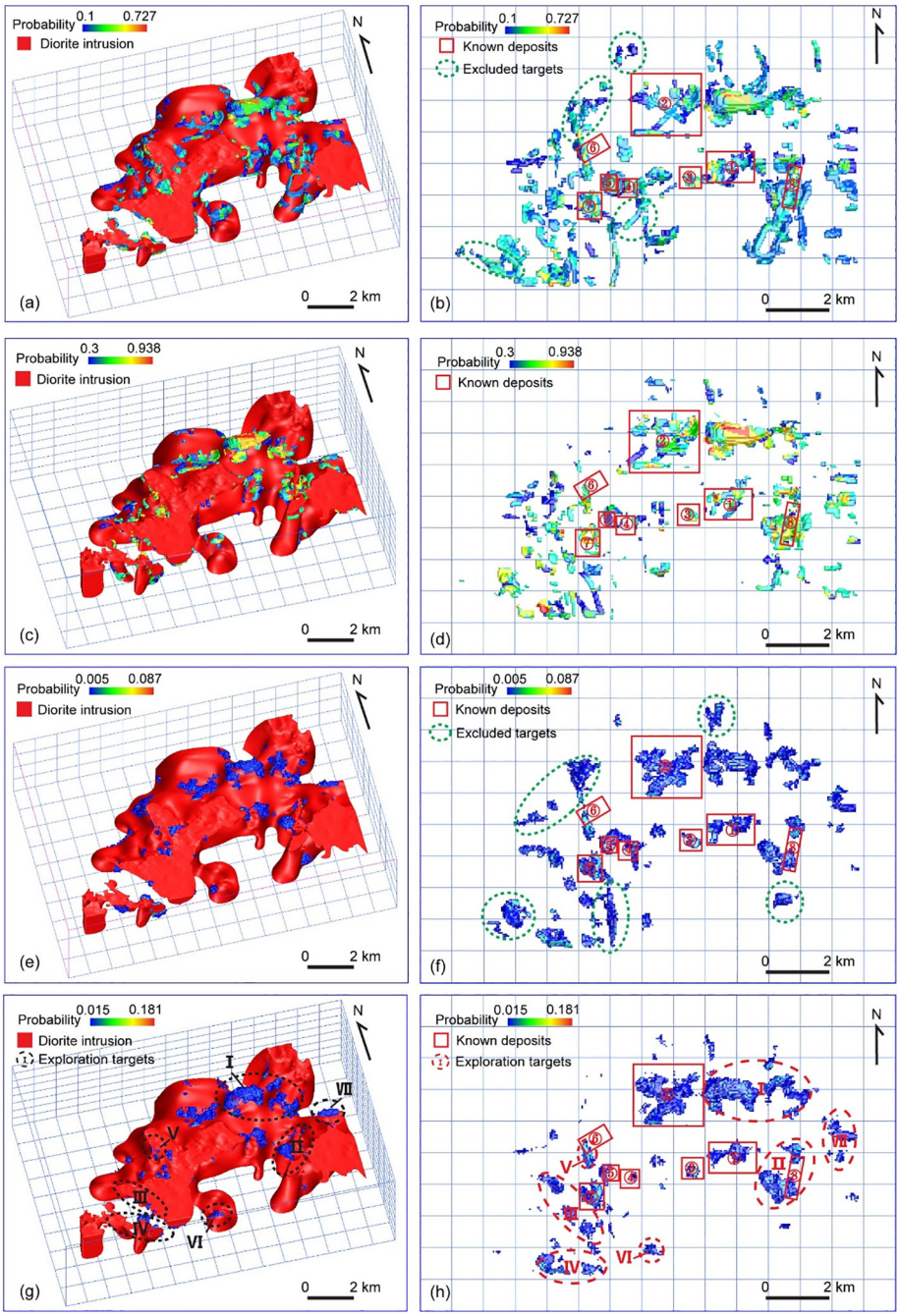

Fig. 21. High-prospectivity areas and exploration targets for skarn-type Fe-Cu mineralization identified during this study based on Dataset B determined using (a, b) weights of evidence and (e, f) logistic regression modeling and based on Dataset A determined using (c, d) weights of evidence and (g, h) logistic regression modeling, respectively. Mineral deposit locations are as follows: (1)- Anqing Cu-Fe deposit, (2)- Zhuchong Fe- Cu deposit, (3)- Matoushan Cu–Fe deposit, (4)- Longmenshan Cu deposit, (5)- Liujiawa Fe-Cu deposit, (6)- Tongniujin Cu–Mo deposit, (7)- LiujiadapaiFe deposit, (8)- Bailin Au deposit.

other prospectivity modeling techniques, including among others the fact that this approach yields easily explained weights that enable the user to identify and quantify spatial relationships between data inputs and mineralization. This modeling requires binary maps as inputs, where continuous 3D predictive maps are binarized using contrast (C) values. These weights and contrast values are given in Table 2 and more details on the binary map generation procedures used during this study are given in Yuan et al. (2014a,b). In contrast, the logistic regression models generated during this study use 3D continuous predictive maps to generate the final prospectivity map in order to preserve as much information as possible.

The results of the logistic regression and weights of evidence prospectivity modeling (Fig. 21) undertaken during this study were assessed using a capture-efficiency curve (Fig. 22; Carranza, 2009; Porwal and Kreuzer, 2010). This approach not only allows the comparison of the targeting performance between predictive Dataset A and B, but also allows the comparison of the targeting performance between logistic regression and weights of evidence modeling. It is clear that the logistic regression modeling is more efficient than weights of evidence modeling regardless of which dataset was used because the curve of the logistic regression modeling envelops larger area. Regardless of whether logistic regression or weights of evidence modeling is used, the models based on Dataset A, which includes the results of the 3D computational simulation, more efficiently identifies areas containing

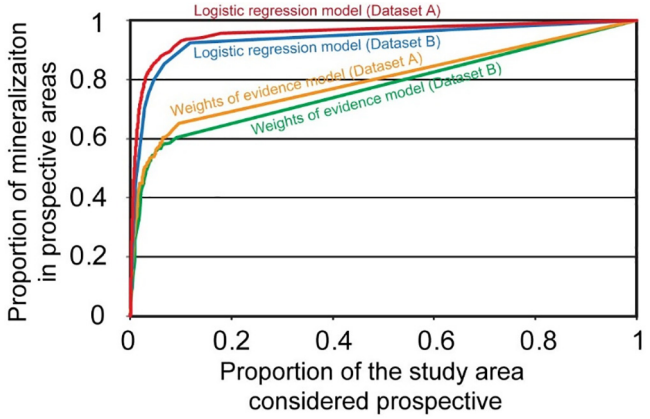

Fig. 22. Capture-efficiency curve for prospectivity modeling based on Dataset A and determined by weights of evidence (yellow) and logistic regression (red) modeling, and Dataset B determined by weights of evidence (green) and Logistic regression (blue) modeling. (For interpretation of the references to colour in this figure legend, the reader is referred to the web version of this article.)

known mineralization as highly prospective areas than Dataset B, which excludes the results of our 3D computational simulation (Fig. 22).

5. Discussion

The results of 3D prospectivity modelling not only delineated areas of known mineralization, but also identified several new exploration targets with large and highly prospectivity areas (I–VII in Fig. 21h) outside of any areas containing known mineralization. It is also important to note that the delineated areas of known mineralization include the Anqing and Zhuchong deposits as well as other known Fe-Cu skarn-type deposits that were not included as training points (Figs. 2 and 21h). In addition, the Longmenshan Cu, Tongniujin Cu-Mo and Bailin Au deposits are not skarn-type deposits and are therefore not associated with any areas of high prospectivity, indicating the importance of correctly selecting exploration criteria and highlighting that our model is specifically focused on the identification of areas prospective for skarn mineralization.

The 3D prospectivity maps generated using logistic regression modeling (Fig. 21h) include areas defined as Targets I and II that we consider to be high priority targets as they represent shallower, larger and more prospective areas of this model. Target I is located to the east of Zhuchong Fe-Cu deposit in an area of doming of the Yueshan and Wuheng dioritic intrusions at an average depth of 400 m (Fig. 21h), meaning this target is shallower than the other targets identified during this study and enabling the relatively easy testing of this target by shallow drilling. Target II is located at depth beneath the known Bailin Au deposit within the lower contact zone between the diorite intrusion and Triassic sediments at an average depth of 1300 m. Drilling associated with the overlying Bailin Au mining area has only reached a depth of 250 m, indicating that deep-seated skarn-type mineralization may exist below the known epithermal Au mineralization in this area. The presence of the known Au deposit and the geochemical and geophysical anomalies associated with this mineralization may also have occluded any anomalous data from this potential target at depth, indicating a need for deeper drilling in this area. Target V is located to the north of the Tongniujin Cu deposit along the contact between the sedimentary Middle Triassic Yueshan Formation and the Yueshan intrusion. Finally, Target IV is located in the southwest of the Yueshan orefield at a depth of > 1400 m. This area remains relatively underexplored, and the previous exploration in this area essentially ignored the potentially mineralized contact between Carboniferous sediments and the diorite intrusion in this area. This contact hosts significant amounts of skarn-type mineralization within the nearby Tongling OCA (Fig. 2), suggesting this contact may also host mineralization within the Yueshan orefield. All of these targets generated by 3D prospectivity modeling highlight the fact that the Yueshan orefield remains highly prospective for exploration for hitherto undiscovered deep-seated skarn-type mineralization. However, we also suggest these targets require deposit-scale geological, geophysical and further 3D prospectivity modeling before any significant drilling is undertaken in order to further reduce exploration risk.

The weight and contrast values determined during weights of evidence modeling (Table 3) are also useful for assessing the importance of individual exploration criteria, and indicate that the most important exploration criteria for the Fe-Cu skarn mineralization in the study area is the geometry of the intrusion. In addition, high dilation zones are also very important exploration criteria, indicating that high dilation zones are closely related to mineralization and demonstrating that 3D computational simulation can provide useful predictive information that can be effectively incorporated into 3D prospectivity modeling to further refine target areas (Fig. 21b and f) to reduce predictive uncertainty and exploration risk.

Finally, although this paper undertook MTH modeling this did not incorporate reactive transport process modeling as a result of limited computational capabilities, the uncertainties involved in determining reaction rates, and the complex nature of the reactive transport process (Meinert et al., 2005). Future research to be undertaken in this area will focus on resolving these issues, enabling the addition of reactive transport modeling to our 3D computational simulation and allowing the more accurate and realistic modeling of ore-forming processes in this area. This in turn will enable improved mineral prospectivity modeling as well as increasing our knowledge of the metallogenic processes that operated in this area.

6. Conclusions

This study presents a 3D prospectivity modeling approach that integrates 3D computational simulation, 3D geological modeling, 3D/2.5D geophysical modeling, and 3D spatial analysis methods to translate conceptual or empirical knowledge to 3D predictive maps. All of the resulting 3D predictive maps were then combined to delineate the location of prospective targets for exploration for concealed mineralization using a data driven modeling approach. The resulting 3D

Table 3
Weight and contrast values generated during weights of evidence modeling.

Exploration criteria	Prospective range	Positive weighting	Negative weighting	Contrast
Contact surface of Carboniferous to Middle Triassic sedimentary units	0–100 (m)	1.270	−0.640	1.910
Diorite contact surface	0–100 (m)	1.706	−0.756	2.462
Faults	0–200 (m)	0.604	−0.385	0.989
Doming and depressions within the diorite intrusion	0–100 (m)	2.471	−0.785	3.256
Tongue shaped sedimentary units	0–200 (m)	1.400	−0.389	1.789
High density geological bodies	0–100 (m)	0.309	−0.125	0.434
High susceptibility geological bodies	0–100 (m)	0.827	−0.425	1.252
High dilation zones	0–200 (m)	1.743	−0.482	2.225

prospectivity models not only clearly identify areas of known mineralization, but also effectively delineated new targets for skarn-type Fe-Cu mineralization at depth within the Yueshan orefield. These include new targets at an average depth of 1300 m beneath the known Bailing Au deposit and associated with the contact between Carboniferous sedimentary formations and diorite intrusions, all of which highlight the potential for future exploration in this region.

Our research indicates the use of the results of 3D computational simulations can enhance the results of 3D prospectivity modeling. However, it is also clear that the current use of 3D predictive maps is still not enough to truly effectively identify targets for mineral exploration. Meeting this challenge will require the extraction of more useful information from 3D computational simulations and 3D geophysical inversion methods, with the resulting data used in conjunction with 3D prospectivity modeling to more effectively and reliably delineate targets as well as reducing uncertainty (and therefore exploration risk).

Acknowledgments

This research was financially supported by funds from the National Natural Science Foundation of China (Grant Nos. 41820104007, 41702353, 41672069), the National Key R&D Program of China (Grant No. 2016YFC0600209), the Fundamental Research Funds for the Central Universities (Grant No. JZ2018HGTB0249), and the China Academy of Science 'Light of West China' Program.

We thank two anonymous reviewers for their careful and constructive reviews of our manuscript and Dr. Mário Gonçalves and Dr. Ignacio González-Álvarez for editorial handling.

Appendix A. Supplementary data

Supplementary data to this article can be found online at https://doi.org/10.1016/j.oregeorev.2018.12.003.

References

326 geological team, 2012, bureau of geology and mineral exploration of Anhui province. Geological report of Zhuchong Fe-Cu deposit, 243.
Abedi, M., Torabi, S.A., Norouzi, G.H., Hamzeh, M., 2012. ELECTRE III: a knowledge-driven method for integration of geophysical data with geological and geochemical data in mineral prospectivity mapping. J. Appl. Geophys. 87, 9–18.
Agterberg, F., Bonham-Carter, G., Wright, D., 1990. Statistical pattern integration for mineral exploration. In: Gaal, G., Merriam, D.F. (Eds.), Computer Applications in Resource Estimation Prediction and Assessment for Metals and Petroleum. Pergamon Press, Oxford, pp. 1–21.
Bonham-Carter, G., 1994. In: Geographic Information Systems for Geoscientists: Modelling with GIS. Elsevier, Oxford, pp. 398.
Bonham-Carter, G., Agterberg, F., Wright, D., 1989. Weights of evidence modelling: a new approach to mapping mineral potential. Stat. Appl. Earth Sci. 89, 171–183.
Calcagno, P., Chilès, J.P., Courrioux, G., Guillen, A., 2008. Geological modelling from field data and geological knowledge: part I. Modelling method coupling 3D potential-field interpolation and geological rules. Phys. Earth Planet. Inter. 171, 147–157.
Carranza, E.J.M., 2004. Weights of evidence modeling of mineral potential: a case study using small number of prospects, Abra, Philippines. Nat. Resour. Res. 13, 173–187.
Carranza, E.J.M., 2009. In: Geochemical Anomaly and Mineral Prospectivity Mapping in GIS. Elsevier, Oxford, pp. 351.
Carranza, E.J.M., Hale, M., 2001. gistic regression for geologically constrained mapping of gold potential, Baguio district Philippines. Ploration Mining Geol. 10, 165–175.
Chang, Y., Liu, X., Wu, Y., 1991. In: The Cu-Fe Metallogenic Belt in the Middle-lower Reaches of Yangtze River. Geological Publish House, Beijing, pp. 379 In Chinese.
Chung, C., Agterberg, F., 1980. Regression models for estimating mineral resources from geological map data. J. Int. Assoc. Math. Geol. 12, 473–488.
Dong, S., Qiu, R., 1993. In Chinese In: Tectonism and Magmatism in the Anqing-Yueshan Area. Geological Publish House, Beijing, pp. pp.
FLAC3D User's Guide, 2012. Version 5.0, Itasca Consulting. Group Inc, Minneapolis, USA.
Harris, D.V.P., 1984. In: Mineral Resources Appraisal: Mineral Endowment, Resources, and Potential Supply. Concepts, Methods and Cases. Oxford University Press, New York, pp. 464.
Jessell, M., 2001. Three-dimensional geological modelling of potential-field data. Comput. Geosci. 27, 455–465.
Jones, M.W., Bærentzen, J.A., Sramek, M., 2006. 3D distance fields: a survey of techniques and applications. IEEE Trans. Visual Comput. Graphics 12, 581–599.
Li, N., Bagas, L., Li, X., Xiao, K., Li, Y., Ying, L., Song, X., 2016. An improved buffer analysis technique for model-based 3D mineral potential mapping and its application. Ore Geol. Rev. 76, 94–107.
Li, Y., Oldenburg, D.W., 1996. 3-D inversion of magnetic data. Geophysics 61, 394–408.
Li, Y., Oldenburg, D.W., 1998. 3-D inversion of gravity data. Geophysics 63, 109–119.
Li, X., Yuan, F., Zhang, M., Jia, C., Jowitt, S.M., Ord, A., Zheng, T., Hu, X., Li, Y., 2015. Three-dimensional mineral prospectivity modeling for targeting of concealed mineralization within the Zhonggu iron orefield, Ningwu Basin, China. Ore Geol. Rev. 71, 633–654.
Lin, H.W., Wang, G.J., 2003. Three dimensional signed euclidean distance transform and its applications. Chin. J. Comput. 26, 1645–1651 [In Chinese with English abstract].
Lindsay, M.D., Aillères, L., Jessell, M.W., de Kemp, E.A., Betts, P.G., 2012. Locating and quantifying geological uncertainty in three-dimensional models: analysis of the Gippsland Basin, southeastern Australia. Tectonophysics 546–547, 10–27.
Lindsay, M.D., Betts, P.G., Ailleres, L., 2014. Data combination and porphyry copper prospectivity models, southeastern Arizona. Ore Geol. Rev. 61, 120–140.
Liu, L., Zhao, Y., Zhao, C., 2010. Coupled geodynamics in the formation of Cu skarn deposits in the Tongling-Anqing district, China: Computational modeling and implications for exploration. J. of Geochem. Explor. 106, 146–155.
Liu, Y., Fan, Y., Yan, S., Si, Z., Zhou, T., 2014b. Petrogensis chronology and evolution of regional magmatic activity study of Anqing-Guichi ore deposit concentrated area in the Middle-Lower Reaches of Yangtze River metallogenic belt. Acta Petrol. Sin. 30, 1117–1129 [In Chinese with English abstract].
Liu, L., Wan, C., Zhao, C., Zhao, Y., 2011. Geodynamic constraints on orebody localization in the Anqing orefield, China: computational modeling and facilitating predictive exploration of deep deposits. Ore Geol. Rev. 43, 249–263.
Liu, L., Zhao, Y., Sun, T., 2012. 3D computational shape- and cooling process-modeling of magmatic intrusion and its implication for genesis and exploration of intrusionrelated ore deposits: an example from the Yueshan intrusion in Anqing. Tectonophysics 526, 110–123.
Liu, L., Sun, T., Zhou, R., 2014a. Epigenetic genesis and magmatic intrusion's control on the Dongguashan stratabound Cu–Au deposit, Tongling, China: evidence from field geology and numerical modeling. J. Geochem. Explor. 44, 97–114.
Lü, Q., Yang, Z., Yan, J., Xu, W., 2007. The metallogenic potential, prospecting idea and primary attempt in depth of the ore belt of the middle and lower reach of the Yangtze River-A Case Study of Tongling Ore District. Acta Geol. Sin. 81, 865–881 [In Chinese with English abstract].
Lü, Q., Qi, G., Yan, J., 2012. 3D geologic model of Shizishan ore field constrained by gravity and magnetic interactive modeling: a case history. Geophysics 78, 25–35.
Malehmir, A., Thunehed, H., Tryggvason, A., 2009. The Paleoproterozoic Kristineberg mining area, northern Sweden: results from integrated 3D geophysical and geologic modeling, and implications for targeting ore deposits. Geophysics 74, 9–22.
Mao, J., Wang, Y., Lehmann, B., Yu, J., Du, A., Mei, Y., Li, Y., Zang, W., Stein, H., Zhou, T., 2006a. Molybdenite Re-Os and albite 40Ar/39Ar dating of Cu-Au-Mo and magnetite porphyry systems in the Yangtze River valley and metallogenic implications. Ore Geol. Rev. 29, 307–324.
Mao, J., Xie, G., Duan, C., Pirajno, F., Ishiyama, D., Chen, Y., 2011. A tectono-genetic model For Porphyry–Skarn–Stratabound Cu–Au–Mo–Fe and magnetite-apatite deposits along the middle-lower Yangtze River Valley, Eastern China. Ore Geol. Rev. 43, 294–314.
Mao, X., Zou, Y., Chen, J., Lai, J., Peng, X., 2006b. In: Three-dimensional Visual Prediction of Concealed Orebodies. Central South University Press, Changsha, pp. 170 In Chinese.
Mao, X., Zhang, B., Deng, H., Zou, Y., Chen, J., 2016. Three-dimensional morphological analysis method for geologic bodies and its parallel implementation. Comput. Geosci. 96, 11–22.
Meinert, L.D., Dipple, G.M., Nicolescu, S. 2005. World Skarn Deposits. Economic Geology 100th Anniversary Volume, 299–336.
Murphy, F., Ord, A., Hobbs, B., Willetts, G., Barnicoat, A., 2008. Targeting stratiform Zn-Pb-Ag massive sulfide deposits in Ireland through numerical modeling of coupled deformation, thermal transport, and fluid flow. Econ. Geol. 103, 1437–1458.
Nielsen, S.H.H., Cunningham, F., Hay, R., Partington, G., Stokes, M., 2015. 3D prospectivity modelling of orogenic gold in the Marymia Inlier, Western Australia. Ore Geol. Rev. 71, 578–591.
Ord, A., Hobbs, B.E., Zhang, Y., Broadbent, G.C., Brown, M., Willetts, G., Sorjonen-Ward, P., Walshe, J.L., Zhao, C., 2002. Geodynamic modelling of the Century deposit, Mt Isa Province, Queensland. Aust. J. Earth Sci. 49, 1011–1039.
Ord, A., Hobbs, B.E., Lester, D.R., 2012a. The mechanics of hydrothermal systems: I. Ore systems as chemical reactors. Ore Geol. Rev. 49, 1–44.
Ord, A., Hobbs, B.E., Lester, D.R., 2012b. The mechanics of hydrothermal systems: I. Ore systems as chemical reactors. Ore Geol. Rev. 49 (8), 1–44.
Payne, C., Cunningham, F., Peters, K.J., Nielsen, S., Puccioni, E., Wildman, C., Partington, G., 2015. From 2D to 3D: prospectivity modelling in the Taupo volcanic zone, New Zealand. Ore Geol. Rev. 71, 558–577.
Perrouty, S., Lindsay, M.D., Jessell, M.W., Aillères, L., Martin, R., Bourassa, Y., 2014. 3D modeling of the Ashanti Belt, southwest Ghana: evidence for a litho-stratigraphic control on gold occurrences within the Birimian Sefwi Group. Ore Geol. Rev. 63, 252–264.
Porwal, A.K., Kreuzer, O.P., 2010. Introduction to the Special Issue: mineral prospectivity analysis and quantitative resource estimation. Ore Geol. Rev. 38, 121–127.
Pressley, A.N., 2010. In: Elementary Differential Geometry. Springer-Verlag, London, pp. 474.
Serra, J., 1986. Introduction to mathematical morphology. Comput. Vision Graphics Image Process. 35, 283–305.
Sprague, K., de Kemp, E., Wong, W., McGaughey, J., Perron, G., Barrie, T., 2006. Spatial targeting using queries in a 3-D GIS environment with application to mineral exploration. Comput. Geosci. 32, 396–418.

Sun, W., Yuan, F., Jowitt, S.M., Zhou, T., Hollings, P., Liu, G., Li, X., 2017. Geochronology and geochemistry of the Fe ore-bearing Zhonggu intrusions of the Ningwu Basin: implications for tectonic setting and contemporaneous Cu-Au mineralization in the Middle-Lower Yangzte Metallogenic Belt. Ore Geol. Rev. 84, 246–272.

Wang, G., Huang, L., 2012. 3D geological modeling for mineral resource assessment of the Tongshan Cu deposit, Heilongjiang Province, China. Geosci. Front. 3, 483–491.

Wang, G., Li, R., Carranza, E.J.M., Zhang, S., Yan, C., Zhu, Y., Qu, J., Hong, D., Song, Y., Han, J., 2015. 3D geological modeling for prediction of subsurface Mo targets in the Luanchuan district, China. Ore Geol. Rev. 83, 270–274.

Weis, P., Heinrich, C.A., 2012. Porphyry-copper ore shells form at stable pressure-temperature fronts within dynamic fluid plumes. Science 338 (6114), 1613–1616.

Williams, N.C., 2008. Geologically-constrained UBC–GIF gravity and magnetic inversions with examples from the Agnew-Wiluna greenstone belt, Western Australia. Ph.D. Dissertation. The University of British Columbia, Kelowna, pp. 488.

Xiao, K., Li, N., Sun, L., Zou, W., Li, Y., 2012. Largc scale 3D mineral prediction methods and channels based on 3D information technology. J. Geol. 36, 229–236 [In Chinese with English abstract].

Xiao, K., Li, N., Porwal, A., Holden, E.J., Bagas, L., Lu, Y., 2015. GIS-based 3D prospectivity mapping: a case study of Jiama copper-polymetallic deposit in Tibet, China. Ore Geol. Rev. 71, 357–367.

Xing, F.M., Xu, Q., 1993. Discovery and significance of the early Proterozoic basement in the middle and lower reaches of the Yangtze River area. Sci. Bull. China 38, 111–118 (in Chinese with English abstract).

Yousefi, M., Carranza, E.J.M., 2016. Data-driven index overlay and boolean logic mineral prospectivity modeling in greenfields exploration. Nat. Resour. Res. 25, 3–18.

Yuan, F., Zhou, T., Wang, S., Fan, Y., Tang, C., Zhang, Q., Yu, C., Shi, C., 2012. Characteristics of alteration and mineralization of the Shaxi porphyry copper deposit, Luzong area, Anhui Province. Acta Petrol. Sin. 28, 3099–3112 (In Chinese with English abstract).

Yuan, F., Li, X., Zhang, M., Jowitt, S.M., Jia, C., Zheng, T., Zhou, T., 2014a. Three-dimensional weights of evidence-based prospectivity modelling: a case study of the Baixiangshan mining area, Ningwu Basin, Middle and Lower Yangtze Metallogenic Belt, China. J. Geochem. Explor. 145, 82–97.

Yuan, F., Li, X., Zhang, M., Zhou, T., Gao, D., Hong, D., Liu, X., Wang, Q., Zhu, J., 2014b. Three dimension prospectivity modelling based on integrated geoinformation for prediction of buried orebodies. Acta Geol. Sin. 88, 630–643 (In Chinese with English abstract).

Zhai, Y., Yao, S., Lin, X., Zhou, X., Wan, T., Jin, F., Zhou, Z., 1992. In: The Metallogeny of the Fe-Cu (Au) Deposits in the Middle-Lower Yangtze Region. Geological Publishing House, Beijing, pp. 235 (In Chinese).

Zhang, L., Zhou, T., Fan, Y., Yuan, F., 2008. SHRIMP U-Pb zircon dating of Yueshan intrusion in the Yueshan ore field, Anhui, and its significance. Acta Petrol. Sin. 24, 1725–1732 (In Chinese with English abstract).

Zhao, C., Hobbs, B.E., Ord, A., Hornby, P., Peng, S., 2008. Morphological evolution of threedimensional chemical dissolution front in fluid-saturated porous media: a numerical simulation approach. Geofluids 8, 113–127.

Zhou, T., Liu, X., Yuan, F., Zhao, Y., Yue, S., 2000. Migrating forms and depositional physicochemical conditions of copper, gold in hydrothermal solutions of Yueshan orefield, Anhui province. Acta Petrol. Sin. 16, 551–558 (In Chinese with English abstract).

Zhou, T., Yuan, F., Yue, S., 2005. In: Petrogenesis and Mineralization of Yueshan orefield, Anhui Province. Geological Publish House, Beijing, pp. 186 (In Chinese).

Zhou, T., Yuan, F., Yue, S., Liu, X., Zhang, X., Fan, Y., 2007. Geochemistry and evolution of ore-forming fluids of the Yueshan Cu–Au skarn- and vein-type deposits, Anhui Province, South China. Ore Geol. Rev. 31, 279–303.

Zhou, T., Wang, S., Fan, Y., Yuan, F., Zhang, D., White, N.C., 2015. A review of the intracontinental porphyry deposits in the Middle-Lower Yangtze River Valley metallogenic belt, Eastern China. Ore Geol. Rev. 65, 433–456.

Zuo, R., Cheng, Q., Agterberg, F.P., 2009. Application of a hybrid method combining multilevel fuzzy comprehensive evaluation with asymmetric fuzzy relation analysis to mapping prospectivity. Ore Geol. Rev. 35, 101–108.